

Nanoscale partitioning of Ru, Ir, and Pt in base-metal sulfides from the Caridad chromite deposit, Cuba

JOSÉ M. GONZÁLEZ-JIMÉNEZ^{1,*}, ARTUR DEDITIUS², FERNANDO GERVILLA^{1,3}, MARTIN REICH⁴, ALEXANDRA SUVOROVA⁵, MALCOLM P. ROBERTS⁵, JOSEP ROQUÉ⁶, AND JOAQUÍN A. PROENZA⁶

¹Departamento de Mineralogía y Petrología, Facultad de Ciencias, Universidad de Granada, Avda. Fuentenueva s/n, 18002 Granada, Spain

²School of Engineering and Information Technology, Murdoch University, Murdoch, 6150 Western Australia, Australia

³Instituto Andaluz de Ciencias de la Tierra (IACT), CSIC-UGR, Avda. de las Palmeras 4, 18100 Armilla, Granada, Spain

⁴Department of Geology and Andean Geothermal Center of Excellence (CEGA), FCFM, Universidad de Chile, Plaza Ercilla 803, Santiago, Chile

⁵Centre for Microscopy, Characterisation and Analysis (CMCA), The University of Western Australia, Perth, 6009 Western Australia, Australia

⁶Departament de Mineralogia, Petrologia i Geologia Aplicada, Universitat de Barcelona (UB), 08028 Barcelona, Spain

ABSTRACT

We report new results of a combined focused ion beam and high-resolution transmission electron microscopy (FIB/HRTEM) investigation of platinum-group elements (PGE)-rich base-metal sulfides. The Ni-Fe-Cu base-metal sulfides (BMS) studied are millerite (NiS), pentlandite [(Ni,Fe)₉S₈], pyrite (FeS₂), and chalcopyrite (CuFeS₂). These BMS were found forming composite inclusions (<60 μm across) within larger unaltered chromite from the Caridad chromite deposit, which is hosted in the mantle section of the Mayarí-Baracoa Ophiolite in eastern Cuba. Electron probe microanalysis of BMS revealed PGE values of up to 1.3 wt%, except for pentlandite grains where PGE concentrations can reach up to 12.8 wt%. Based on the amount of Ru, two types of pentlandite are defined: (1) Ru-rich pentlandite with up to 8.7 wt% of Ru and <3.5 wt% of Os, and (2) Ru-poor pentlandite with Ru <0.4 wt% and Os <0.2 wt%. Ru-rich pentlandite contains Ir-Pt nanoparticles, whereas the other sulfides do not host nanometer-sized platinum-group minerals (PGM). The Ir-Pt inclusions are found as: (1) idiomorphic, needle-shape (acicular) nanoparticles up to 500 nm occurring along the grain boundaries between Ru-rich pentlandite and millerite, and (2) nanospherical inclusions (<250 nm) dispersed through the matrix of Ru-rich pentlandite. HRTEM observations and analysis of the selected-area electron diffraction patterns revealed that nanoparticles of Ir-Pt form domains within Ru-rich pentlandite. Fast Fourier transform analyses of the HRTEM images showed epitaxy between Ir-Pt domain and PGE-poor millerite, which argues for oriented growth of the latter phase. These observations point to sub-solidus exsolution of the Ir-Pt alloy, although the presence of nanospherical Ir-Pt inclusions in some other grains suggest the possibility that Ir-Pt nanoparticles formed in the silicate melt before sulfide liquid immiscibility. These Ir-Pt nanocrystals were later collected by the sulfide melt, preceding the formation of Ru-rich pentlandite. Early crystallization of the Ru-rich pentlandite and Ir-Pt nanoparticles led to the efficient scavenging of PGE from the melt, leaving a PGE-poor sulfide residue composed of millerite, pyrite, chalcopyrite, and a second generation of PGE-poor pentlandite.

Keywords: Nanoparticles, platinum-group elements (PGE), focused-ion beam (FIB), transmission electron microscopy (TEM), chromite, Cuba; Applications of Fluid, Mineral, and Melt Inclusions

INTRODUCTION

The potential role of nanometer-sized phases during the selective partitioning of platinum-group elements (PGE: Os, Ir, Ru, Rh, Pt, and Pd) has been little explored, particularly under the high temperatures that are typical for magmatic processes. Previous experimental studies carried out in binary mixtures of pure metals indicate that Ir and Pt can form alloys with a face-centered cubic (fcc) structure over a range of temperatures ranging from 975 to 1370 °C (Turchi et al. 2006 and references therein). This is consistent with the fact that Pt-bearing Ir alloys phases have been indeed documented in natural samples.

For example, Pt-bearing Ir alloys (with trace amounts of Os) have been found associated with laurite (RuS₂) or pentlandite [(Ni,Fe)₉S₈] in mantle peridotites (e.g., Lherz massif in France and Horoman Complex in Japan; Kogiso et al. 2011; Lorand et al. 2010), chromite ores from the Oman ophiolite (Ahmed and Arai 2003) and in magmatic platinum-group mineral nuggets found in rivers draining ultramafic-mafic complexes of the Goodnews Bay in Alaska (e.g., Tolstykh et al. 2002). Additionally, nanometer-sized particles of Ir-bearing Pt alloys have been observed within pentlandite grains in chromite ores from the Bushveld Complex in South Africa (Wirth et al. 2013).

Experimental studies by Peregoedova et al. (2004) show that monosulfide solid solution (*mss*) with variable amounts of Pt, Ir, and Pd can exsolve discrete Ir-Pt alloys particles during desulfurization (i.e., decrease of sulfur fugacity, f_{S_2}) at magmatic

* E-mail: jmgonzj@ugr.es

† Special collection papers can be found online at <http://www.minsocam.org/MSA/AmMin/special-collections.html>.

temperatures (~1000 °C). Based on this observation, Lugué and Reisberg (2016) suggested that Ir-Pt-(Os) alloys associated with BMS in mantle peridotite were most likely exsolved from a precursor PGE-bearing *mss*, which had experienced desulfurization at high temperatures during partial melting. The exsolution of (sub)micrometric Ir-Pt-(Os) from base-metal sulfides may have also resulted from desulfurization of a PGE-bearing *mss* due to redox changes of the mantle (Jugo 2009) or interaction with percolating S-undersaturated melt/fluids (Lorand et al. 2010). In contrast, experiments in the Fe-Cu-S-(Pt+As) system and mineralogical observation of PGE ores from the Bushveld Complex provide evidence that Pt-rich nanoparticle formation may precede crystallization of the host *mss* (Helmy et al. 2013; Wirth et al. 2013; Junge et al. 2015). More recently, Fonseca et al. (2017) reported the formation of Ir-Pt alloys (>100 µm across) in equilibrium with Ni-rich sulfide melts during experiments. These observations suggest that Ir-Pt alloys may crystallize directly from silicate melts, either before or contemporaneously with the segregation of immiscible sulfide melts. In fact, Finnigan et al. (2008) synthesized nanometer-sized Ir-Pt nanocrystals from basaltic melts in experiments involving the crystallization of chromite, at the P - T - f_{O_2} conditions relevant for the formation of chromite deposits in the upper mantle (i.e., 0.5 GPa, T ~1300–1400 °C, and f_{O_2} at FMQ; see Fig. 4a in Finnigan et al. 2008). However, it is important to note that the aforementioned experiment was carried out in the absence of sulfur, therefore hindering the formation of Ir-Pt alloys within sulfides.

The previous data show that the relationship between Pt-rich Ir alloys and magmatic sulfides is still poorly understood. In particular, the mechanism(s) and relative timing of Ir-Pt alloy crystallization during magmatic evolution remains elusive, especially when sulfides are present. This contribution aims to fill this gap of knowledge by providing a detailed characterization of a suite of micrometer- to nanometer-sized Ir-Pt alloy inclusions hosted within Ni-rich sulfides from the Caridad chromite deposit in eastern Cuba. This study stems from a recent report by González-Jiménez and Reich (2017) reporting the occurrence of Ir-Pt nanoalloys at the interface between pentlandite and secondary heazlewoodite [Ni₃S₂] in the altered zones of the chromite from this deposit. These aforementioned authors preliminarily suggested a magmatic origin for these nanoalloys, although this hypothesis was not confirmed on the basis of the available data. Here we present a nanoscale characterization of the Ir-Pt alloy inclusions and the sulfide host matrix, obtained by combining focused ion beam micro-sampling techniques with high-resolution transmission electron microscopy (HRTEM) observations and electron microprobe analysis (EPMA). Our study explores the origin of Ir-Pt nanoparticles in natural samples, providing new insights to unravel the often complex relations between noble metal alloy formation, sulfide melt segregation and chromite crystallization in high-temperature ore system.

SAMPLES AND METHODS

The samples analyzed in this study were collected from the podiform chromitite ore body of Caridad in the Sagua de Tánamo district, eastern Cuba (Fig. 1; Proenza et al. 1999; Gervilla et al. 2005; González-Jiménez et al. 2011, 2012).

The Sagua de Tánamo area is a small mining district (~3 km long), located in the northern part of the Mayari-Cristal massif that, together with the Moa-Baracoa massif to the east, constitute the Mayari-Baracoa Ophiolitic Belt (MBOB) (Marchesi et al.

2006; Proenza et al. 2006). The Mayari-Cristal massif represents a piece of mantle wedge suprasubduction-zone, which formed close to the Greater Antilles paleo-island arc 90 Ma ago (Proenza et al. 2006; Marchesi et al. 2006, 2007, 2011). The mantle sequence of the Mayari-Cristal massif consists mainly of highly depleted harzburgite and subordinate concordant lenses and layers of dunite, all intensively serpentinized (Proenza et al. 2003). Dikes of gabbros and pyroxenites with island arc tholeiitic affinity crosscut these peridotites (Marchesi et al. 2006). The Caridad chromitite body is hosted in a dunite lens lying concordantly with this mantle harzburgite. The samples analyzed in this study are banded-textured chromitites collected from the external part of the ore body; they are almost entirely unaltered, although some chromite grains exhibit narrow alteration to ferrian chromite along edges or late crosscutting fractures filled with serpentine. To ensure a magmatic origin of PGM inclusions, this study focused exclusively in grains that were fully hosted in unaltered chromite.

Compositional analyses of the PGE-bearing inclusions and their host sulfides were acquired using a JEOL 8530F electron probe microanalyzer (EPMA) equipped with five tunable wavelength-dispersive spectrometers at the Centre of Microscopy, Characterization and Analysis (CMCA), University of Western Australia. Operating conditions were 40° take-off angle, an accelerating voltage of 20 kV, a beam current of 20 nA, with the beam fully focused to 1 µm diameter. Elemental data were acquired during two analytical sessions. The following analyzing crystals were used: LiF for FeK α , RuL α , TeL α , CuK α , NiK α , CoK α , CrK α , SnL α , HgL α , ReL α , OsL α , IrL α , and PtL α ; PETJ for RhL α , SK α , AgL α , PdL α , and RuL α ; PETH for MoL α , PbM α , SbL α , and BiM α ; and TAP for SiK α , AsL α , and SeL α . The counting time was 20–30 s for all elements and mean atomic number (m.a.n.) background correction was used for all elements (Donovan et al. 1996, 2016). The standards were Cr₂O₃ for CrK α ; galena for PbM α ; Bi₂Se₃ for SeL α ; Ag metal for AgL α ; Cu metal for CuK α ; wollastonite for SiK α ; Mo metal for MoL α ; Co metal for CoK α ; Bi metal for BiM α ; Pt metal for PtL α ; metal Sb for SbL α ; arsenopyrite (Asp200) for AsL α ; cassiterite

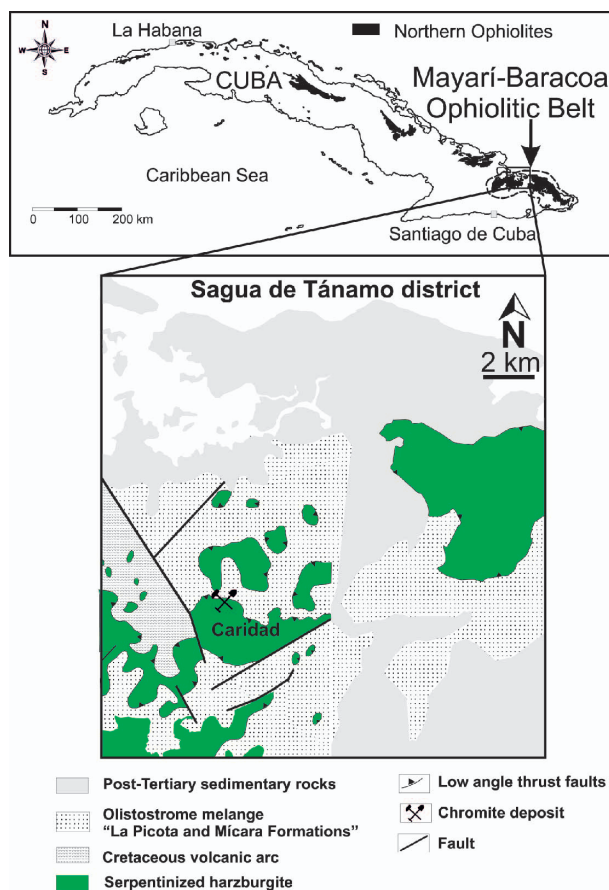


FIGURE 1. Location of the Caridad chromitite in the northern part of the Mayari-Cristal Massif and simplified geological map of the area (modified from González-Jiménez et al. 2012). (Color online.)

for SnLα; Au metal for AuLα; millerite for SKα and NiKα; chalcopyrite for FeKα; Ru metal for RuLα; Rh metal for RhLα; Pd metal for PdLα; Os metal for OsLα; Ir metal for IrLα; Re metal for ReLα; and synthetic HgTe (coloradoite) for TeLα and HgLα. On peak interference corrections were applied as appropriate (Donovan et al. 1993). Unknown and standard intensities were corrected for deadtime. For both sessions, a quantitative blank correction was utilized (Donovan and Tingle 1996). The Phi-Rho-Z algorithm utilized was Armstrong/Love Scott (Armstrong 1988). Maximum detection limits for each element are provided in Supplemental¹ Table 1.

Elemental mapping were acquired at an accelerating voltage of 20 kV and a beam current of 80 nA. Pixel dimensions were between 0.25 and 0.10 μm, depending on the size of the grain of interest. The dwell time per pixel was 200 ms. The calibration run used for map post-acquisition processing was similar to that for the point analyses given above. The raw count data was processed using the CalcImage application and output for further enhancement using Golden Software's Surfer program. Maximum detection limits for the analyzed elements were: S = 0.2 wt%, Fe = 0.1–0.15 wt%, Cu = 0.2–1.0 wt%, As = 0.3–0.4 wt%, Ir = 0.8–1.0 wt%, Ru = 0.4–0.6 wt%, Rh = 0.3–0.4 wt%, Pt = 0.8–1.0 wt%, and Pd = 0.3–0.4 wt%.

In situ Re-Os analyses of the BMS were carried out by González-Jiménez et al. (2012) at GEMOC (Macquarie University, Australia) using Wave/Merchantek UP 213 laser microprobe with a modified ablation cell coupled with a Nu Plasma Multicollector ICP-MS. Measurements were made in static collection mode by using two combinations of collectors: (1) masses 194, 192, 190, 189, 188, 187, 186, and 185 in Faraday cups, and (2) masses 194, 193, 192, 191, 190, 189, 188, and 186 in Faraday cups and 187 and 185 in ion counters. The all-Faraday configuration allows the simultaneous measurement of Os, Re, and Pt, and the repositioning of the ion beams by changing the magnet field and zoom lens voltages to direct masses 187 and 185 into ion counters allows Ir to be measured. During the analyses the laser was fired at a frequency of 5 Hz, with energies of 1–2 mJ/pulse and a spot size of 20–80 μm. A standard NiS bead (PGE-A) with 199 ppm Os (Lorand and Alard 2001) and ¹⁸⁷Os/¹⁸⁸Os = 0.1064 (Pearson et al. 2002) was analyzed between samples to monitor any drift in the Faraday cups and ion counters. These variations typically were less than 0.1% over a long day's analytical session. During the analyses, a dry aerosol of Ir was bled into the gas line between the ablation cell and the ICP-MS to provide a mass-bias correction with a precision independent of the abundance of Os in the unknown. The data were collected using the Nu Plasma time-resolved software, which allows the selection of the most stable intervals of the signal for integration. The selected interval was divided into 40 replicates to provide a measure of the standard error. Under the ablation conditions described above, signal intensities (0.02–1.4 V) obtained give a range of precision for ¹⁸⁷Os/¹⁸⁸Os from 2×10^{-4} to 2×10^{-3} (2 SE); these values are quite similar to, or better than, that obtained for the PGE-A standard.

The thin-foil samples were prepared by using FEI Helios NanoLab G3 CX DualBeam and focused ion beam (FIB) at the Center for Microscopy, Characterization and Analysis (CMCA), University of Western Australia. Sections prepared using the Helios G3 were extracted from the sample surface by in situ lift-out, welded onto a copper grid, thinned to electron transparency with a 30 kV ion beam where the beam current was progressively reduced from 2.5 to 0.23 nA, and then finally polished with a 5 kV beam with a 41 pA current. Subsequently, the samples were analyzed by using a Titan G2 80-2090 transmission electron microscope (TEM) with ChemiSTEM technology at 200 kV.

RESULTS

Base-metal sulfide assemblages

The BMS studied here include millerite (NiS), pentlandite [(Ni,Fe)₉S₈], pyrite (FeS₂), and chalcopyrite (CuFeS₂) (Figs. 2–4). They form isolated grains enclosed by unaltered magmatic chromite away from visible fractures or the contact with the serpentinized silicate matrix of the chromite (Figs. 2a–2h). The BMS inclusions are up to 60 μm across and have polyhedral (rarely spherical) shape and sharp boundaries with the host chromite. Sporadically, millerite occurs as single isolated grains. Polyphase aggregates consist of millerite associated with pentlandite ± Ru-rich pentlandite ± pyrite ± chalcopyrite (Figs. 2a–2d), whereas the biphasic ones consist of millerite with pentlandite, pyrite, or chalcopyrite (Figs. 2c–2h). Interestingly, pyrite is found as bleb-like inclusions in millerite grains or at their rims; the latter microstructural position is also characteristic of chalcopyrite.

Quantitative WDS X-ray element maps also reveal differences

of PGE contents in the individual sulfide grains forming a given composite solid inclusion (Fig. 3). These noble metals are distributed homogeneously within the matrix of the hosting minerals or form submicrometer-sized particles of mainly Ir and Pt (Fig. 3).

Supplemental¹ Table 1 and Figures 4a–4f show results of EPMA analyses BMS. All the analyzed base-metal sulfides show Fe, Ni, Cu, and S close to ideal stoichiometry and overall total PGE concentrations up to 1.3 wt%, with the exception of a few Ru-rich pentlandite grains (up to 12.8 wt%; Supplemental¹ Table 1 and Figs. 4c–4f). Based on their Ru content, two types of pentlandite were identified, Ru-rich and Ru-poor. The Ru-rich pentlandite is richer in Ru and Os (up to 8.67 and 3.53 wt%, respectively) than Ru-poor pentlandite (Ru < 0.4 wt% and Os < 0.2 wt%; Figs. 4c–4d). Millerite contains up to 3 wt% of Fe, 0.07 wt% of Os and Ru and 0.05 wt% of Rh (Fig. 4e). Pentlandite (up to 42.2 wt% of Ni) is characterized by a moderate variation in Ni/Fe ratios (1.6–2.1). Pyrite has up to 0.08 wt% of Os and 0.05 wt% of Ru; the concentration of Au in pyrite is as high as 0.12 wt%. Chalcopyrite also is depleted in Ir, Pt, and Pd; however, it has the highest contents of Rh (up to 0.4 wt%). Osmium and Ru in chalcopyrite are up to 0.7 wt% and <0.07 wt%, respectively (Supplemental¹ Table 1).

Structure of platinum-group minerals and base-metal sulfides

The re-examination of the time-resolved spectra signals collected during LA-MC-ICP-MS analyses of Re-Os isotopes of the same samples by González-Jiménez et al. (2012) revealed the presence of abundant ¹⁹⁴Pt spikes (Fig. 5). The ¹⁹⁴Pt spikes is noticeable as the signal of main components of the host sulfide decreases rapidly (Fig. 5). This observation is consistent with the BSE images suggesting that Pt-rich alloys are not always fully enclosed by the sulfide matrix (Fig. 2b). These are single-phase grains with acicular (up to 10 × 5 μm) and bleb-like (<500 nm) shape that are associated with Ru-rich pentlandite often along the contact between this later Ni-Fe sulfide and millerite (Figs. 2a, 2b, and 3), or single sphere-like, nanometer-sized grains (<250 nm) that are widespread throughout the matrix of Ru-rich pentlandite (Figs. 2c–2d). WDS X-ray maps obtained by EPMA revealed that these particles contain Ir and Pt.

One FIB thin foil (Figs. 6a–6e) was cut perpendicular to the grain boundaries between Ir-Pt alloy, Ru-rich pentlandite, and millerite of the grain shown in Figures 2a and 3a–3f. The cross section revealed a triangular shape of Ir-Pt particle, reaching a depth of 250 nm (Fig. 6a). The TEM-EDS elemental mapping of the area containing all three phases revealed a better association between Ir, Pt, Os, and Cu in the Ir-Pt particle. In addition, the particle contains Fe, Co, Ru, and S, although Ni is below detection. All elements in the Ir-Pt particle and within the associated sulfides are homogeneously distributed (Fig. 5). Ru and Co are also enriched in Ru-pentlandite relative to millerite (Fig. 6a). The high concentrations in Ru, Co, and Fe in the Ir-Pt particle and in the coexisting Ru-rich pentlandite is also reflected by a diffuse contact between both minerals (Figs. 6b and 6d). Bright-field (BF) and high-resolution (HR) TEM observations, and fast Fourier transform analyses (FFT) of the HRTEM images revealed that all three minerals are crystalline (Figs. 6b–6e). Fast Fourier transformation of the HRTEM images

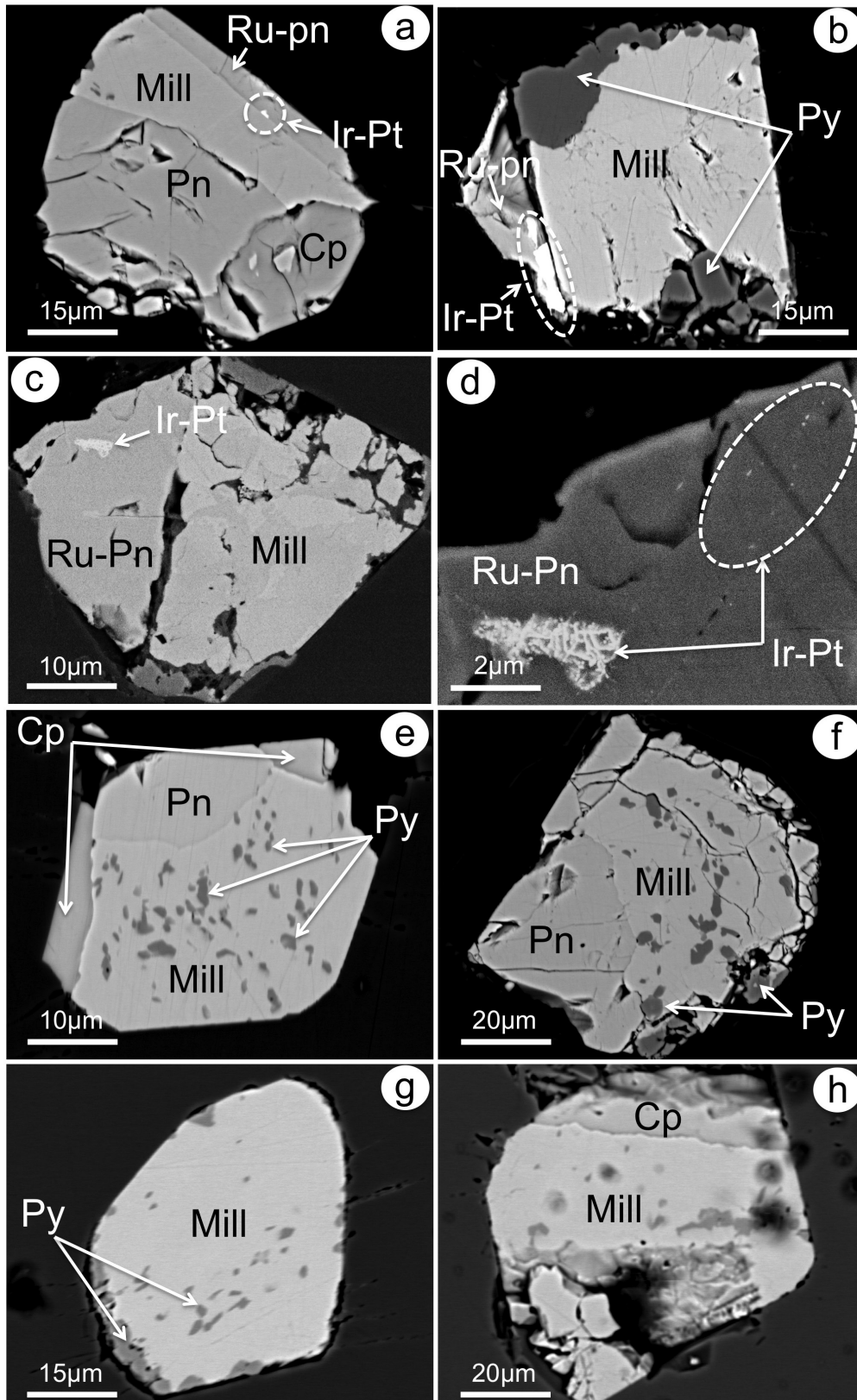


FIGURE 2. Backscattered electron images base-metal sulfides hosted within unaltered chromite grains from the Caridad chromite deposit in Cuba. Ir-Pt nanoparticles are also shown. Mill = millerite; Pn = pentlandite; Cp = chalcocopyrite; Py = pyrite; Ru-Pn = Ru-rich pentlandite.

of the Ir-Pt nanoparticle showed that it is a single crystal, similar in its structure to Ru-pentlandite and millerite (Figs. 6c–6e). The HRTEM investigations of the grain boundary between the Ir-Pt particle and the Ru-rich pentlandite show continuous lattice fringes within a single crystal, and FFT revealed structural continuity (Fig. 6d). This strongly suggests that Ir-Pt particle is a nanometer-sized domain within the Ru-rich pentlandite. In addition, the relative decrease in the Fe and Ni concentration in Ir-Pt domain compared to the Ru-rich pentlandite matrix suggests that PGE+Co+Cu substitute for Fe and Ni in the Ru-rich pentlandite. Epitaxy was found between the Ir-Pt domain and

millerite. However, a small misorientation between the structure of the Ir-Pt domain and millerite is documented by discoidal diffused diffraction maxima (Fig. 6e).

DISCUSSION

Origin of base-metal sulfides

Based on their textural position within chromite it is proposed that BMS were trapped during the formation of the hosting mineral (e.g., Garuti et al. 1999; Malitch et al. 2001; González-Jiménez et al. 2012). The idiomorphic morphology of some of these grains suggest free crystallization from a

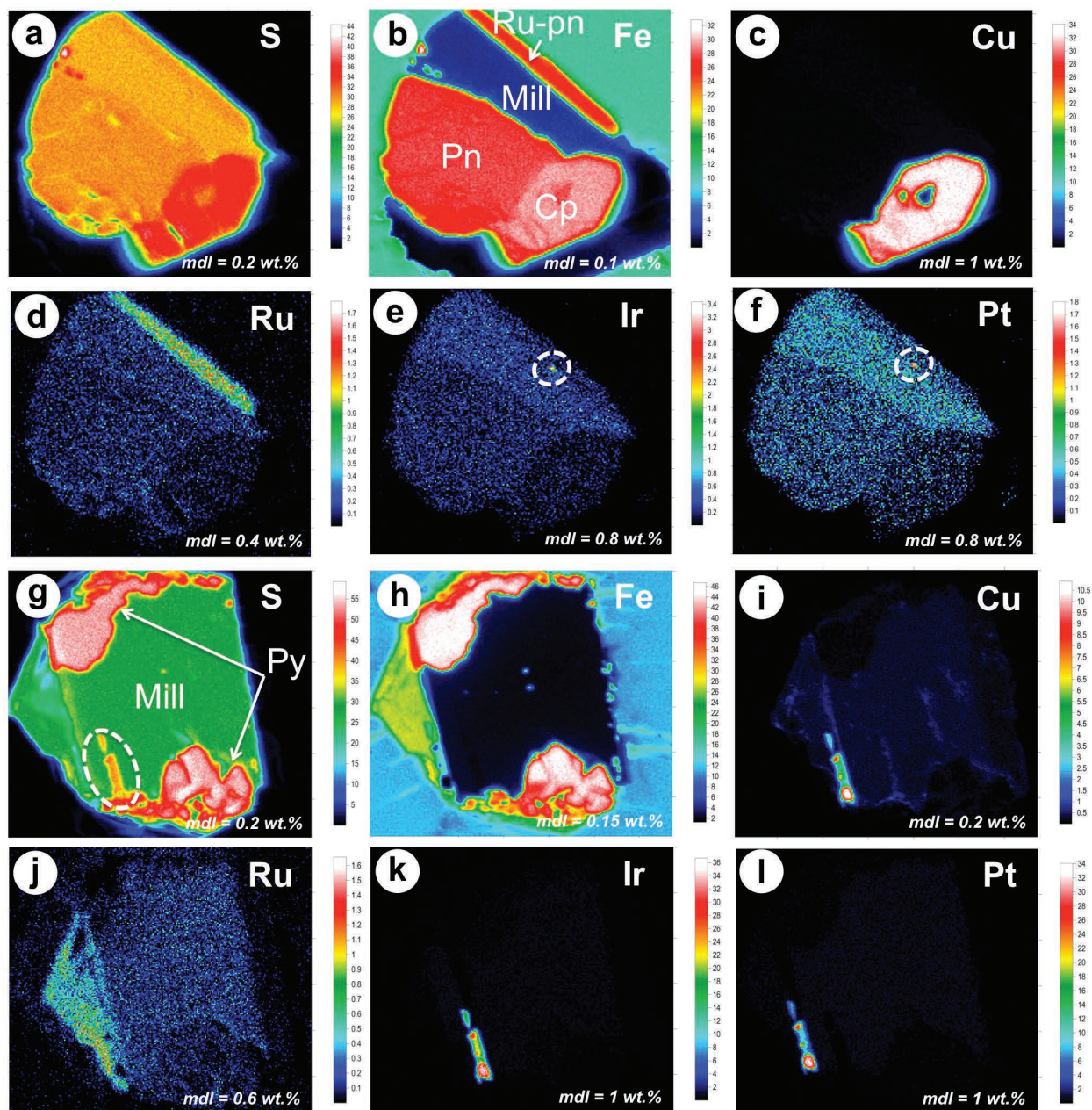


FIGURE 3. Wavelength-dispersive spectrometry (WDS) X-ray elemental maps of base-metal sulfide assemblages. (a–f and g–l) The solid composite inclusions in Figures 1a and 1b, respectively. Color scale bars show element concentrations in wt%; mdl = minimum detection limit. Single-spot EPMA analyses of this grain correspond to those named as CAR-1-B1 a to w provided in Supplemental¹ Table 1. (Color online.)

melt prior to chromite (e.g., Fig. 2b). In contrast, drop-like or anhedral inclusions may indicate their crystallization from liquid or a mixture of liquid and suspended microcrystallites that were mechanically trapped by growing chromite (e.g., Fig. 2e). These solid inclusions of BMS consist of single isolated grains of millerite, often associated with polyphasic or biphasic aggregates of pentlandite \pm pyrite \pm chalcopyrite (Figs. 2a–2h). Even though immiscible sulfide melts were segregated before or contemporaneously to chromite crystallization (\sim 1000–1200 °C; Hill and Roeder 1974; Ballhaus 1998), most the observed sulfide assemblages were not present during formation, due to the lower thermal stability of pentlandite, pyrite, and chalcopyrite (e.g., Kullerud 1962, 1963; Makovicky et al. 1986; Sugaki and Kitakaze 1998; Ballhaus et al. 2001; Naldrett et al. 2009).

Several experiments in the Fe-Ni-S system have shown

that a Fe-rich *mss* is the first solid phase to crystallize after the immiscible segregation of a sulfide liquid from a silicate melt above 1000 °C (Fig. 6a; Kullerud 1962, 1963; Chang and Hsieh 1986; Ebel and Naldrett 1996; Fleet 2006). With a temperature decrease to around \sim 610 °C, the metal excess in the *mss* is exsolved as pentlandite (Fig. 7b). This assemblage of *mss*+pentlandite is stable down to 300 °C, below which the *mss* decomposes into several sulfides of Ni and Fe, including millerite and pyrite that may coexist with pentlandite (Figs. 6c and 6d; Shewman and Clark 1970; Misra and Fleet 1973; Craig 1973; Fedorova and Sinyakova 1993). In some of the studied inclusions of the Caridad deposit (e.g., Fig. 2b) millerite, pentlandite, and pyrite exhibit mutual contacts suggesting that they have reached equilibrium. Phase relations in the system Fe-Ni-S system predict that this mineral assemblage

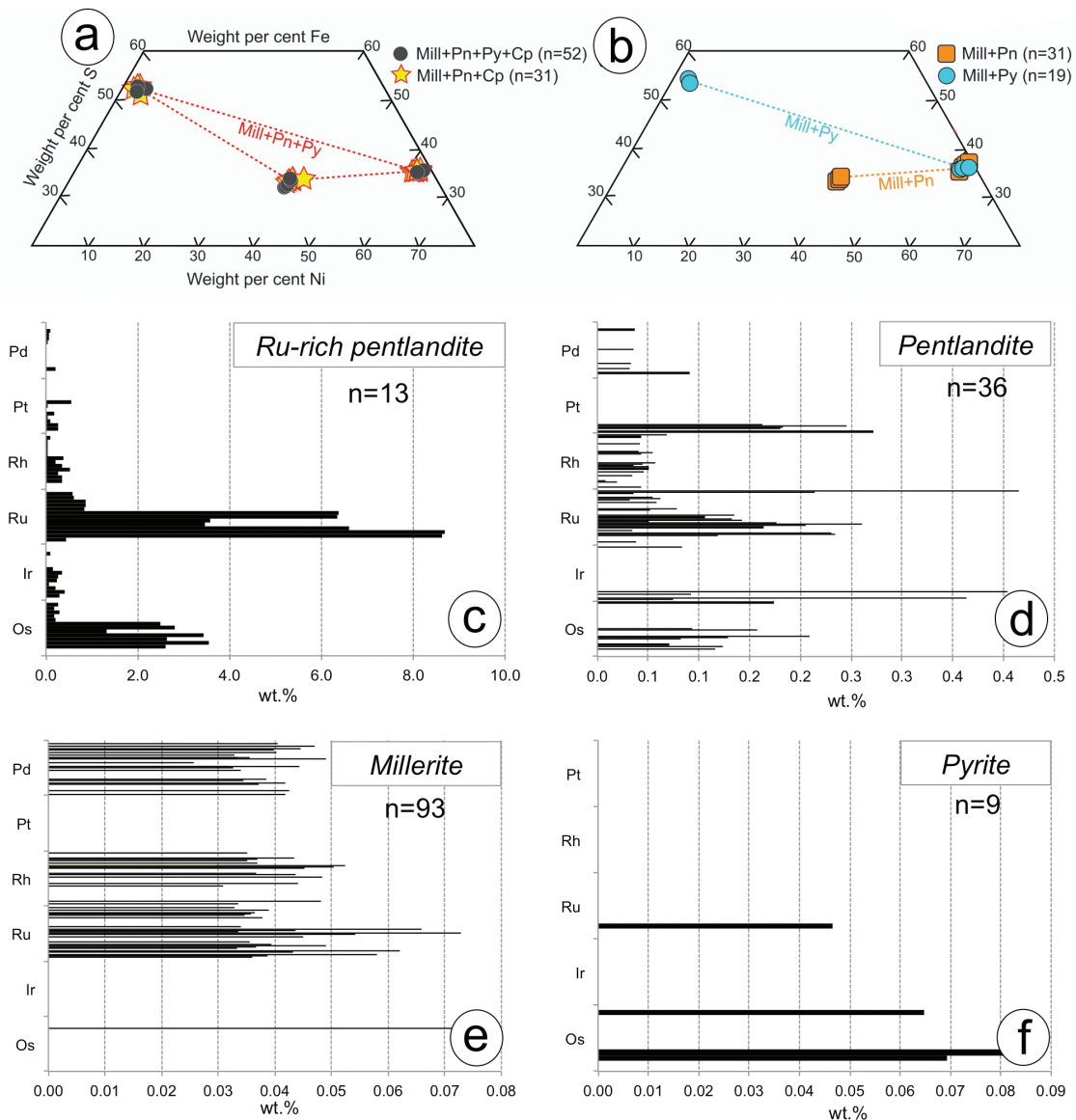


FIGURE 4. Chemical composition of the base-metal sulfides in terms of Ni, Fe, and S (a–b) and PGE (c–f). Note that in c–f each bar shown in the histogram represents a single EPMA spot analysis. (Color online.)

is stable at $\sim 135\text{--}100\text{ }^{\circ}\text{C}$ (Fig. 7d). In contrast, in some other composite inclusions of millerite+pentlandite+pyrite, pyrite occurs as blebby inclusions in millerite, but not in contact with pentlandite. There are different possibilities to explain these textural types.

The first possibility is the incomplete decomposition of the original *mss* during its subsolidus subsolidus re-equilibrium. Another possible explanation for the presence of blebby pyrites in millerite (e.g., Figs. 2e–2g) is that the precursor Fe-rich *mss* has also undergone significant chemical readjustment but through a different fractional pathway. This original Fe-rich *mss* could be depleted in iron before or once it was sealed in chromite. This would occur as result of the preferential partitioning of Fe^{2+} into chromite (Finnigan et al. 2008), either when minute droplets of sulfide melt were segregated along the silicate melt-chromite interface or trapped in the oxide. In this scenario the composition of the *mss* is shifted toward the Ni-S join of the Fe-Ni-S system (Naldrett et al. 1989, 2009), giving rise in an extreme case to a nearly stoichiometric Ni_{1-x}S (Fig. 8a). This phase that may contain up to 5 wt% Fe has a $\alpha\text{-NiS}$ structure, which should have been inverted to the low-temperature millerite structure (i.e., $\beta\text{-}\alpha\text{-NiS}$) at $379\text{ }^{\circ}\text{C}$ (Kullerud and Yund 1962). In this scenario, minute bleb-like pyrite in some millerite grains (e.g., Figs. 2e–2g) may reflect an excess of Fe in the Ni-sulfide, which was exsolved at the temperature of the polymorphic change. The same final product could be achieved if millerite had crystallized directly from a sulfide melt instead of a product of high-temperature subsolidus re-equilibration of the

mss. Metal-sulfide equilibrium in the Ni-Fe-S system (Wood 1987) indicates that the high-temperature polymorph of millerite $\alpha\text{-NiS}$ is stable at temperatures ($1000\text{--}1200\text{ }^{\circ}\text{C}$) and sulfur fugacity ($\log f_{\text{S}_2}$ from -0.5 to 1) relevant for the crystallization in the upper mantle (Fig. 8b). Early crystallization of $\alpha\text{-NiS}$ directly from melts also can explain the presence of single millerite crystals with or without pyrite inclusions. Moreover, crystallites of millerite might have been trapped in solid state together with some volumes of sulfide liquids during the formation of the chromitite by melt mixing (González-Jiménez et al. 2012). In this scenario, solid and liquids may have reacted producing the variety of composite inclusions of millerite (with or without pyrite) \pm pentlandite \pm chalcocopyrite (e.g., Figs. 2a–2h). The origin of pentlandite in these latter inclusions may be associated with the partial reaction of the sulfide liquid with the $\alpha\text{-NiS}$ phase. In support of this interpretation, a series of experiments (Sugaki and Kitakaze 1998; Kitakaze et al. 2016) have demonstrated that a high-form of pentlandite can be produced as a result of the pseudoperitectic reaction between Ni-rich liquid and *mss* in the Ni-Fe-S system at $\sim 870\text{ }^{\circ}\text{C}$. This high-form of pentlandite coexists with *mss* and/or liquid at $\sim 870\text{--}739\text{ }^{\circ}\text{C}$ (Fig. 8c), and its re-equilibration persists to temperatures of about $625\text{ }^{\circ}\text{C}$, below which it undergoes transformation into the low-form of pentlandite.

The association of chalcocopyrite with Ni-Fe sulfides in some of the studied composite grains (Figs. 2a, 2c, and 2e) points to the Cu-rich compositions. Experimental data on the Fe-Ni-Cu system (Craig and Kullerud 1969; Fleet and Pan 1994; Ballhaus et al. 2001) have shown that *mss* is the first phase that crystallizes from a Fe-Ni-Cu sulfide melt once it has separated by liquid immiscibility from a mafic silicate melt (Fig. 9a). At $1000\text{ }^{\circ}\text{C}$, this *mss* coexists with a Cu-rich melt that may incorporate variable amounts of Ni (Craig and Kullerud 1969; Ballhaus et al. 2001). At $\sim 900\text{ }^{\circ}\text{C}$, the Cu-rich residual liquid crystallizes to intermediate solid solution (*iss*), so at this point there is a Ni-rich portion and a Cu-rich portion (Fig. 9b). According to the experiments of Craig and Kullerud (1969) at $850\text{ }^{\circ}\text{C}$ the *mss* (with up to 30 wt% Ni) already coexists with chalcocopyrite (Fig. 9b), whereas below $850\text{ }^{\circ}\text{C}$ the *mss* breaks down into several sulfides developing a variety of two- and three-phase regions. In this system, assemblages made up of $\alpha\text{-NiS}$ and chalcocopyrite are stable equilibrium $\sim 830\text{ }^{\circ}\text{C}$ (Craig and Kullerud 1969 and references therein); these are interpreted as the precursors of the biphasic grains of millerite+chalcocopyrite shown in Figure 2e. As the temperature cools $<600\text{ }^{\circ}\text{C}$, the *mss* recrystallizes to pentlandite giving rise to the assemblages of pentlandite+chalcocopyrite assemblage (Fig. 2a).

The above observations suggest that some of the inclusions in the Caridad deposit may have evolved along different fractionation pathways involving the formation of *mss* and *iss* upon cooling. The differences in the mineralogical composition of the sulfide aggregates, namely the presence of chalcocopyrite suggests derivation from droplets of immiscible sulfide melts with distinctly different contents of Ni, Fe, and Cu, and different metal/sulfur ratios. Once sealed within the chromite, these sulfide melt inclusions would have evolved as individual closed systems, following different fractional pathways depending on the original composition of the primitive sulfide liquid.

Fate of PGE during crystallization of Fe-Ni sulfide inclusions

The textural relationships observed in some composite solid inclusions made up of Ir-Pt domain in Ru-rich pentlandite

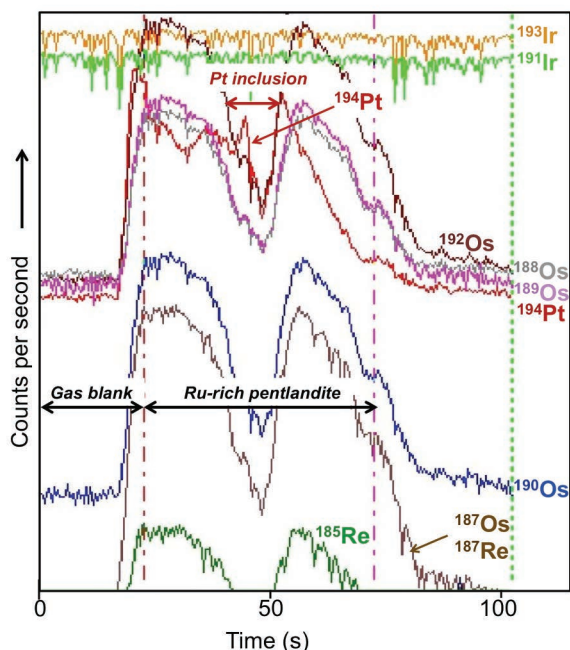


FIGURE 5. Representative time-resolved LA-MC-ICP-MS spectra collected during Re-Os analysis of Ru-rich pentlandite (González-Jiménez et al. 2012). The transient spectrum of ^{194}Pt shows a peak that is interpreted as a Pt-bearing inclusion. Despite that Pt-dominated inclusions associated with Caridad sulfides contain Ir, the isotopes of this element did not change in the time-resolve spectra because and monitoring Ir-bearing solution was introduced during ablation (see Pearson et al. 2002). (Color online.)

and other BMS indicate that some of the small droplets of immiscible sulfide melts rich in base metal segregated at high temperature (≥ 1000 °C) were also enriched in PGE. This observation is also supported by the relatively high PGE contents detected in single-spot analyses and quantitative X-ray maps obtained using EPMA of some of the BMS (Figs. 3 and 4c–4f and Supplemental¹ Table 1). The contents of PGE within a given BMS mineral in Caridad varies from one inclusion to another (Figs. 4c–4f and Supplemental¹ Table 1), thus provid-

ing additional support for the hypothesis that several droplets of sulfide melts with their own inherited PGE melt/sulfur ratio were trapped by growing chromite.

In the polyphasic aggregates in Figures 2a and 3a–3f, pentlandite in contact with the Ir-Pt domain is enriched in Ru (up to 6200 ppm), whereas the other BMS of the inclusion have PGE concentrations close to or below detection (Supplemental¹ Table 1). The polyphasic aggregate of millerite+Ru-rich pentlandite+pyrite+Ir-Pt-(Rh-Cu) of Figures 2b and

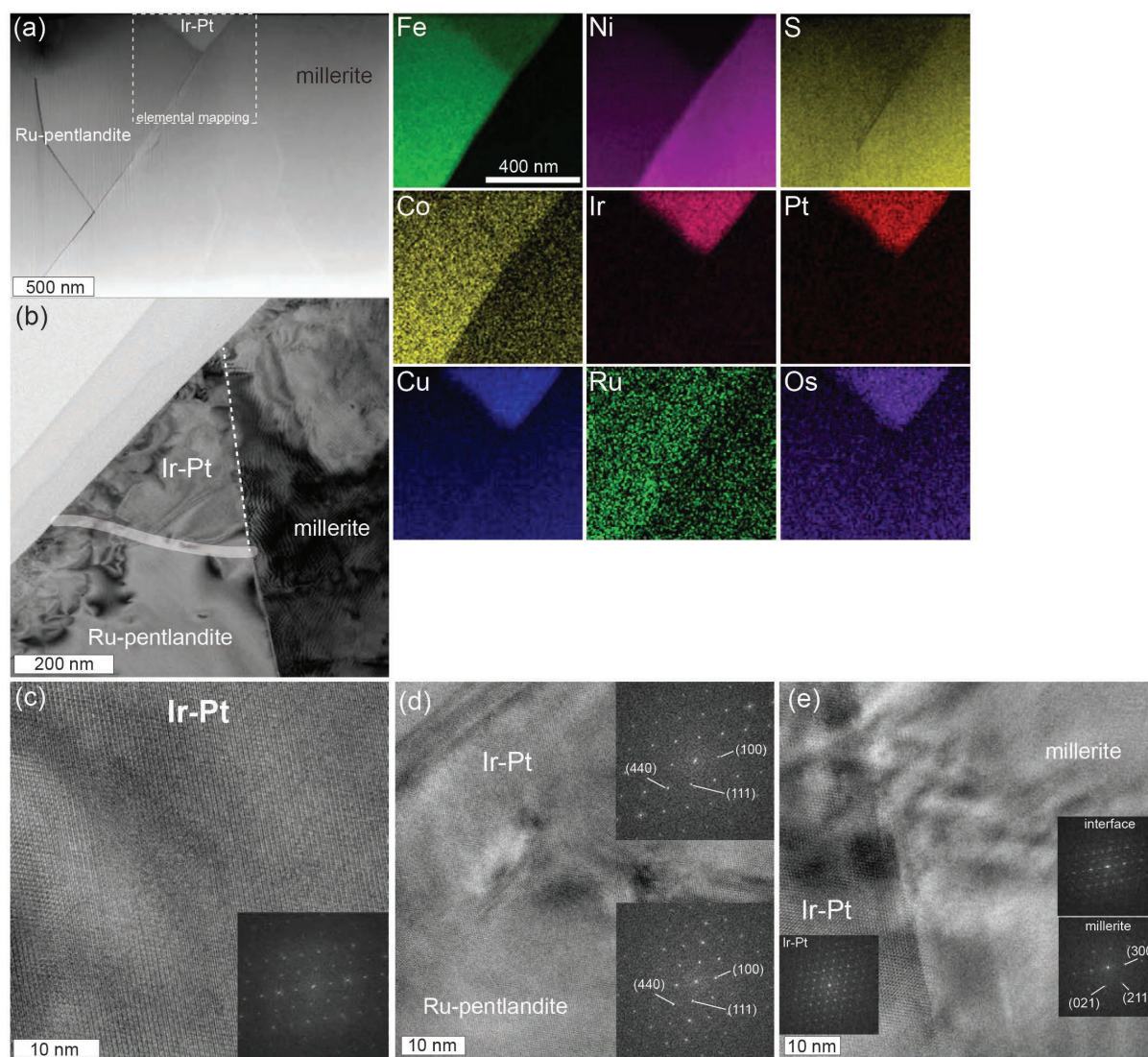


FIGURE 6. TEM images of Ru-rich pentlandite, millerite, and Ir-Pt nanoparticle (grain shown in Figs. 1a and 2a–2f). (a) HAADF-STEM image shows a triangular Ir-Pt nanoparticle in contact with Ru-rich pentlandite and millerite. The EDS maps on the right-hand side show the chemical composition of the selected area in **a** indicating: (1) relative enrichment and homogeneous distribution of Ru and Co in Ru-rich pentlandite and the Ir-Pt nanoparticle, with respect to millerite; (2) correspondence between Fe, Ir, Pt, Cu, and Os in the Ir-Pt nanoparticle; and (3) relative depletion in Ni in the Ir-Pt nanoparticle with respect to millerite and pentlandite. (b) Low-magnification BFTEM image of sharp grain boundaries between Ir-Pt and millerite (dashed line), and diffused grain boundary between Ir-Pt and Ru-rich pentlandite (gray thick line). (c) HRTEM image of a single Ir-Pt domain, with its associated diffraction pattern obtained by fast Fourier transformation (FFT). (d) HRTEM image of the grain boundary between the Ir-Pt domain and the Ru-pentlandite matrix, and its FFT diffraction pattern. (e) HRTEM image showing the continuous boundary between Ir-Pt domain and millerite. Inset shows the FFT images of the Ir-Pt nanoparticle, the millerite matrix and the interface between the two. (Color online.)

3g–3l exhibit a similar distribution of PGE, with pentlandite associated with the Ir-Pt domain being enriched in Ru (Fig. 3j) while the other sulfides within the inclusion are strongly depleted in PGE (Figs. 3j–3l). TEM observation of Ir-Pt domains shows the same structure and relative enrichment in Co and Ru as the Ru-rich pentlandite matrix (Figs. 6a–6e). This suggests that the alloy was separated from the PGE-rich sulfide during cooling. However, the relatively low content of PGE in the sulfide host (<6200 ppm Ru) was not enough to promote the exsolution of Ir-Pt-Ru domains as lamellae with preferred crystallographic orientation. In fact, Ir and Pt are randomly distributed in the sulfide matrix as attest to the fact that Ru-rich pentlandite of the studied FIB foil does not exhibit additional diffraction maxima between the major Bragg reflections. For example, Junge et al. (2015) observed that pentlandite of the Bushveld Complex contain Rh- and Ir-rich lamellae only in those domains where the concentration of Rh in the pentlandite matrix was as high as 12.3 wt%. On the other hand, concentrations of Co and PGE (up to

620 ppm Ru in 3 analyses out of 11 for this grain; Supplemental¹ Table 1) are about one order of magnitude lower in millerite than in Ru-rich pentlandite, indicating its later crystallization in a system that was already depleted in these elements. This is consistent with the observation that PGE-depleted millerite has the same crystallographic orientation as the Ir-Pt domains within Ru-rich pentlandite, thus indicating epitaxial growth with some structural misfit at the boundary and accumulation of strain (Figs. 6b and 6e).

The TEM observations show that the Ru-rich pentlandite containing the Ir-Pt domain fractionated the PGE available into solid solution during the early crystallization stages, leaving behind a PGE-depleted BMS residue. At the Caridad deposit, the PGE originally contained in the silicate melt were mostly fractionated into droplets of immiscible sulfide melt, containing Ni, Fe, Cu, after sulfide saturation. Under equilibrium conditions, the PGE concentrations of the sulfide droplets are estimated to be at least 10 000 times higher than in the coexisting silicate melt

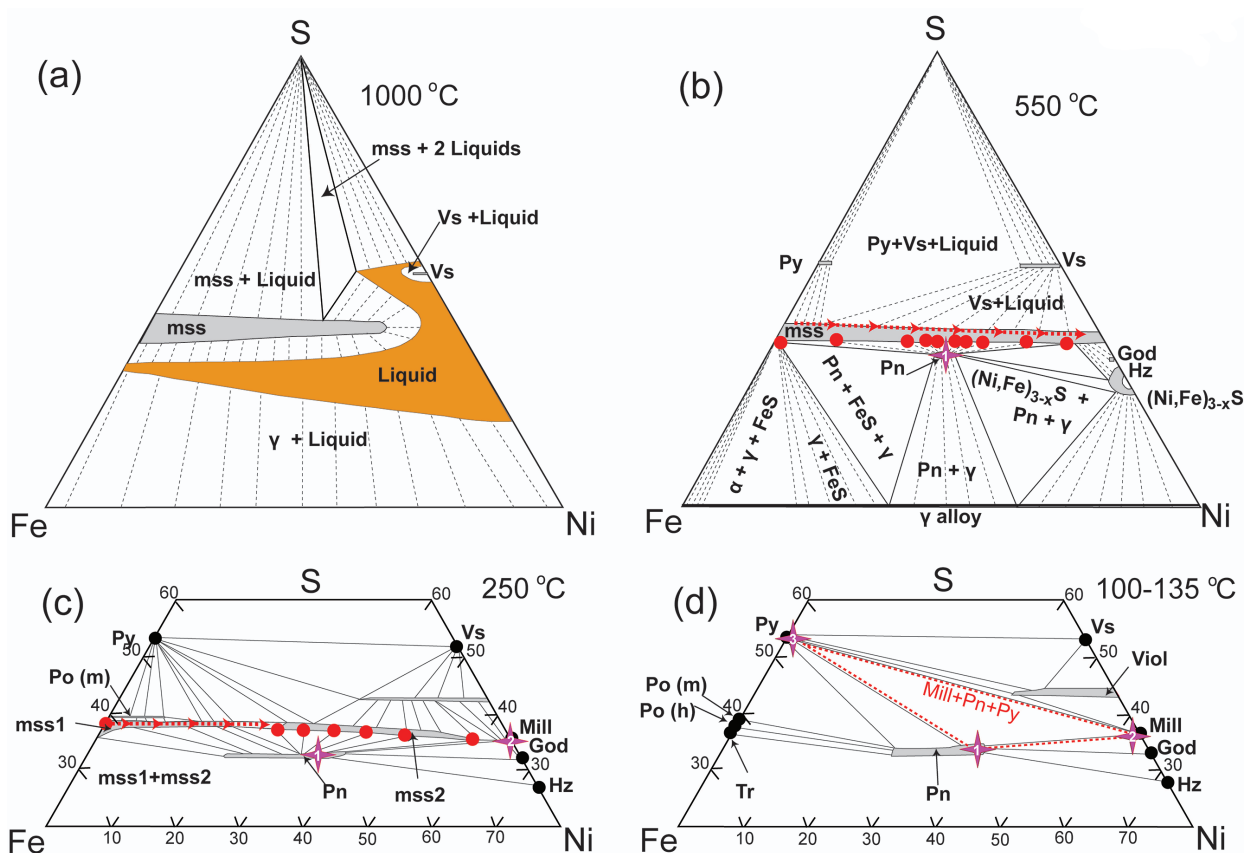


FIGURE 7. Phase relations (1 bar) in the Fe-Ni-S system at 1000 °C (a), 550 °C (b), 250 °C (c), and 135–100 °C (d). The plots were modified from Kullerud and Yund (1962), Craig (1973) and Naldrett et al. (2009). Keys: *mss* = monosulfide solid solution [(Fe,Ni)_{1-x}S], *Vs* = vaesite (NiS₂), *Po*(m) = monoclinic pyrrhotite (Fe_{1-x}S), *Po*(h) = hexagonal pyrrhotite (Fe_{1-x}S), *Tr* = troilite (FeS), *Py* = pyrite (FeS₂), *Pn* = pentlandite [(Ni,Fe)₉S₈], *Vio* = violarite (FeNi₂S₄), *Mill* = millerite (NiS), *god* = godlevskite (Ni₇S₆), *Hz* = heazlewoodite (Ni₃S₂). At 100 °C *mss* already coexists with Ni-Fe liquid (a), whereas at 550 °C pentlandite (purple star-1) derived from the subsolidus recrystallization of the *mss* at 610 °C is present. (b) Arrows in the dotted red line indicate the possible pathway of progressive enrichment in Ni of *mss* upon cooling, as a result of Fe exchange between the base-metal sulfide inclusion and the larger chromite host (e.g., Naldrett et al. 1989). In this plot, the red dots indicate all possible compositions of *mss* in equilibrium with pentlandite at the given temperature. At temperatures below 300 °C, *mss* decomposes into various 2- and 3-phase assemblages. Millerite (purple star-2) is stable with pentlandite at 250 °C (c), while complete equilibrium of composite assemblages of millerite + pentlandite + pyrite (purple star-3), as those shown in Figure 2b are only stable at much lower temperatures (135–100 °C) (d). (Color online.)

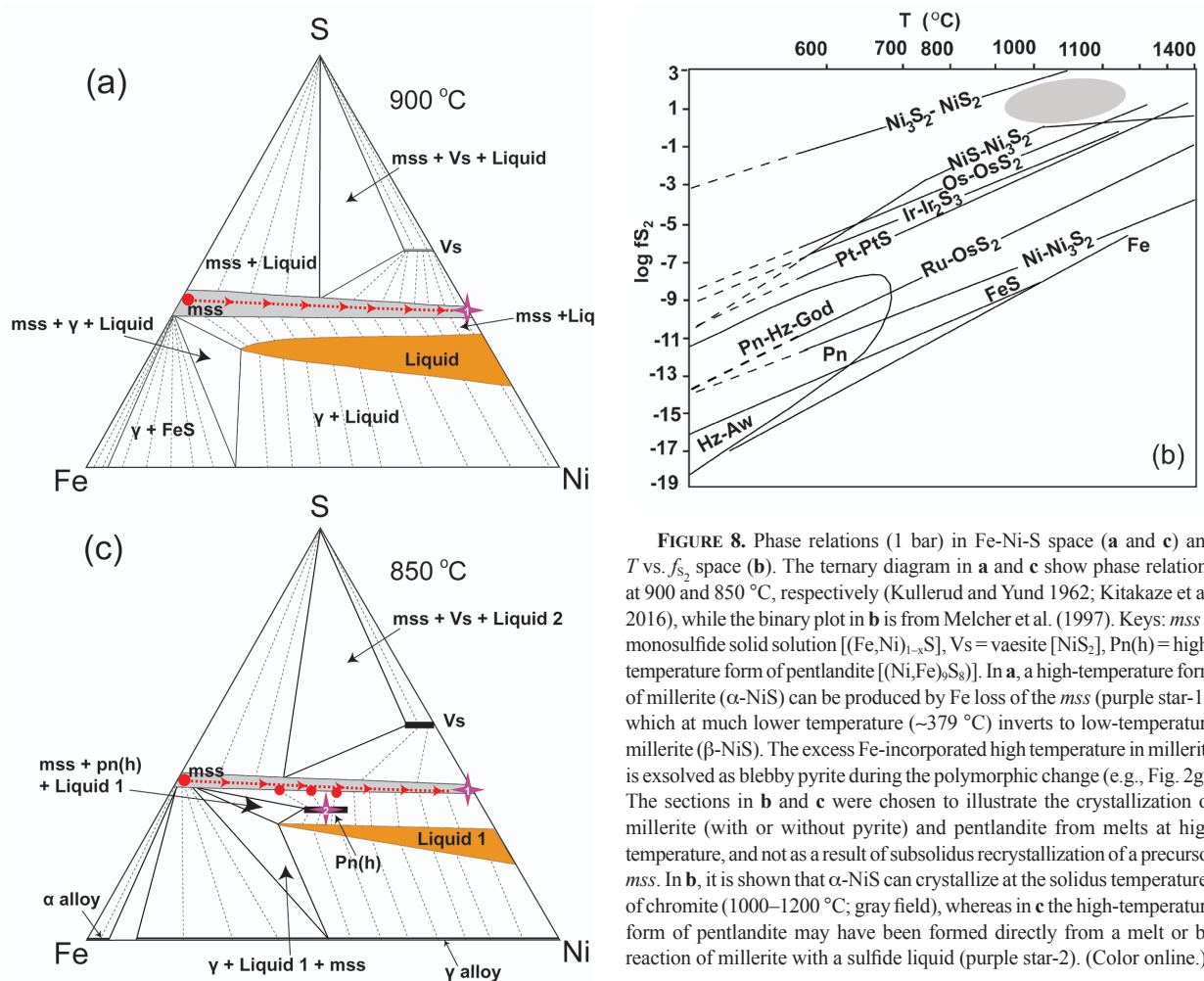


FIGURE 8. Phase relations (1 bar) in Fe-Ni-S space (**a** and **c**) and T vs. f_{S_2} space (**b**). The ternary diagram in **a** and **c** show phase relations at 900 and 850 °C, respectively (Kullerød and Yund 1962; Kitakaze et al. 2016), while the binary plot in **b** is from Melcher et al. (1997). Keys: *mss* = monosulfide solid solution [(Fe,Ni)_{1-x}S], *Vs* = vaesite [NiS₂], *Pn(h)* = high-temperature form of pentlandite [(Ni,Fe)₈S₈]]. In **a**, a high-temperature form of millerite (α -NiS) can be produced by Fe loss of the *mss* (purple star-1), which at much lower temperature (\sim 379 °C) inverts to low-temperature millerite (β -NiS). The excess Fe-incorporated high temperature in millerite is exsolved as blebby pyrite during the polymorphic change (e.g., Fig. 2g). The sections in **b** and **c** were chosen to illustrate the crystallization of millerite (with or without pyrite) and pentlandite from melts at high temperature, and not as a result of subsolidus recrystallization of a precursor *mss*. In **b**, it is shown that α -NiS can crystallize at the solidus temperatures of chromite (1000–1200 °C; gray field), whereas in **c** the high-temperature form of pentlandite may have been formed directly from a melt or by reaction of millerite with a sulfide liquid (purple star-2). (Color online.)

structure of pentlandite to retain Ir and Pt as solid solution also decreases (Makovicky et al. 1986, 1988, 1990). This structural re-arrangement promoted the formation of a discrete Ir-Pt-(Os-Cu) domains as observed in Figures 2a and 2b. However, and as noted above, the PGE content was not high enough to result in a complete structural ordering and exsolution of PGE lamellae, such as e.g., Rh-rich lamella observed in Rh-rich pentlandite from the Bushveld Complex (Junge et al. 2015).

On the other hand, the Cu-rich melt that coexisted with the *mss* at approximately 1000 °C should have still contained appreciable amounts of Ni (Figs. 9a–9b). This PGE-depleted sulfide liquid was very likely the parental melt for the assemblage of PGE-poor pentlandite \pm millerite \pm pyrite \pm chalcopyrite coexisting with Ru-rich pentlandite shown in Figures 2a and 2b. This interpretation is consistent with experimental data and observations in natural samples showing that when pentlandite forms early from a PGE-rich *mss*, it inherits most of the PGE, whereas coexisting millerite, pyrite, and chalcopyrite concentrates little or no PGE (Piña et al. 2012 and references therein). In this model, the exsolution-induced formation of discrete Ir-Pt alloy must have occurred soon after the formation of pentlandite but before

(Fleet et al. 1999; Holwell et al. 2015). Furthermore, *mss*/sulfide melt partition coefficient (Li et al. 1996; Ballhaus et al. 2001; Mungall et al. 2005) and empirical observations in several Ni-Cu and PGE ore deposits (Piña et al. 2012, 2016; Barnes and Ripley 2016) suggest that the IPGE (i.e., Os, Ir, Ru) and Rh would partition into the early-formed *mss* leaving a Cu-rich residual liquid enriched in Pt and Pd. In contrast, our observations suggest that in the Caridad chromite deposit the precursor *mss* concentrated most of the PGE leaving behind a Cu-rich residual liquid depleted Pt and Pd. Interestingly, the experiments by Peregoedova et al. (2004) showed that *mss* can concentrate significant amounts of Pt, Ir, and Pd in solid-solution at high temperatures (at least 0.2 wt%). Available LA-ICP-MS data from *mss* (regardless of its Ni- or Fe-rich composition) hosted in mantle peridotite indicate support these experimental results indicating that *mss* can effectively concentrate both IPGE and PPGE (i.e., Pt, Pd, Rh) in solid solution at high temperatures (e.g., Wang et al. 2009; González-Jiménez et al. 2014; Saunders et al. 2015; Tassara et al. 2017). In the Caridad chromite deposit, as temperature decreased to around 610 °C, the metal excess in the precursor PGE-rich *mss* would have been exsolved to PGE-rich pentlandite (Figs. 7a and 7b). With decreasing temperature, the ability of the

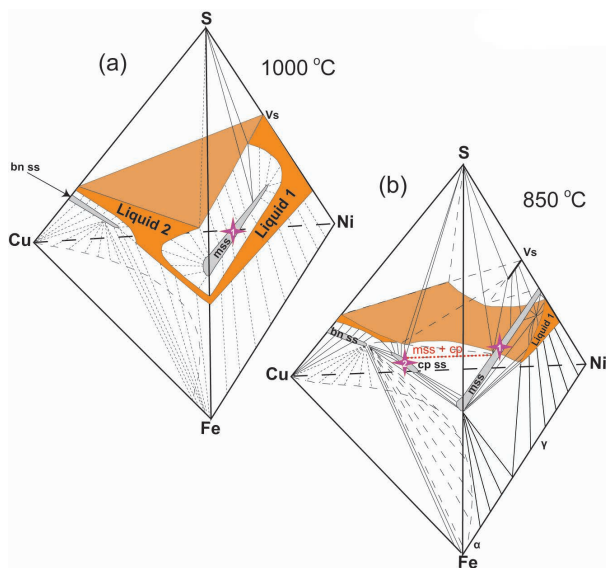


FIGURE 9. Phase relations (1 bar) in the sulfur-rich portion of the Cu-Fe-Ni-S system at 1000 °C (a) and 850 °C (b) (Craig and Kullerud 1969; Cabri 1973). Keys: *mss* = monosulfide solid solution [(Fe,Ni)_{1-x}S], *Vs* = vaesite (NiS₂), *bn ss* = bornite solid solution (CuFe₂S₃), *cp ss* = chalcopyrite solid solution (CuFeS₂). Note that in a, the *mss* (purple star-1) coexists with two liquids at 1000 °C (a Ni-Fe-rich liquid in the Ni-Fe-S portion and a Cu-rich liquid in the Cu-Fe-S portion). At 850 °C, the *mss* coexists with chalcopyrite (purple star-2), as indicated by the dotted red line. (Color online.)

millerite, as shown by the structural relationship between Ir-Pt domain and millerite (Fig. 6).

Figures 2c–2d shows a very different scenario. In this composite grain made up of millerite associated with Ru-rich pentlandite (with up to 8.67 wt% Ru and 3.53 wt% Os) there are two types of nanoparticles of Ir-Pt: nanometer-sized (<250 nm) particles with a preferred crystallographic orientation and a larger single fibrous grain ~2 μm across. Unlike the scenario discussed before, the relatively high PGE content of this pentlandite matrix may have favored the formation of discrete and oriented PGE-bearing lamellae, as a result of the low-temperature exsolution. In contrast, the fibrous texture of the larger Ir-Pt particles may reflect the coalescence of several sub-microscopic particles of these noble metals. The coarsening of Ir-Pt particles is expected to occur with an increase in temperature favoring diffusion and growth by Ostwald ripening (e.g., Reich et al. 2006; González-Jiménez et al. 2015) and not upon cooling when the efficiency of diffusional processes are dramatically decreased, particularly below 300 °C (Brenan et al. 2000; Fonseca et al. 2017). Thus, it is very likely that Ir-Pt particles were segregated during the crystallization of chromite (e.g., Finnigan et al. 2008) and later entrained by sulfide droplets once sulfide saturation was achieved in the basaltic melt, similar to observations in other natural samples and experiments (e.g., Tredoux et al. 1995; Ballhaus and Sylvester 2000; Wirth et al. 2013; Laurenz et al. 2013; Helmy et al. 2013). The formation of the Ir-Pt nanoparticles is expected in the silicate melt due the strong tendency of these two metals to form nuggets in high-temperature silicate melts (~1500–1200 °C; Amossé et al. 1990; Borisov and Palme 1995,

1997). The results of the experiments carried out by Borisov and Palme (1997) indicate that once suspended in the silicate liquid, Ir and Pt will rapidly react to form Ir-Pt alloys owing their higher alloy/sulfide partition coefficient than the other PGE (Peregoedova et al. 2004; Fonseca et al. 2017). This siderophile behavior is strongly reinforced when chromite crystallizes from the melt, as the stability of pure Ir and Pt are strongly dependent of f_{O_2} changes in the silicate melt, induced by chromite crystallization (Mungall 2005; Matveev and Ballhaus 2002; Bockrath et al. 2004). The results of Finnigan et al. (2008) confirm this observation where Ir-Pt nanocrystals (~700 nm in diameter) were crystallized directly from basaltic melt at the P - T - f_{O_2} conditions relevant for the formation of chromite deposits in the upper mantle, i.e., 0.5 GPa, $T \approx 1300$ – 1400 °C and f_{O_2} at FMQ. Under these conditions, sub-micrometric Ir-Pt particles might have been suspended in the silicate melt or attached to growing chromite crystals as metallic, oxygen, or sulfur-bearing compounds (Wirth et al. 2013). If these Ir-Pt nanoparticles were originally captured by the sulfide melt, as soon as the *mss* crystallized they should have been adhered to the solid phase due to their wetting properties. Aggregation and coalescence of these nanoparticles would produce larger Ir-Pt nanocrystals that might growth to micrometric-sized Ir-Pt (e.g., Figs. 2c–2d; Fonseca et al. 2017). Therefore, the occurrence of Ir-Pt-oriented nanoparticles in the Ru-rich pentlandite would reflect the preferential clustering of these particles along growth planes in pentlandite (Wirth et al. 2013; Junge et al. 2015). This interpretation points to the fact that PGE fractionation is not exclusively dependent on the sulfide-silicate or *mss*/sulfide liquid partition, but may be also influenced by other factors including physical separation and collection of previously crystallized nanoalloys (Ballhaus et al. 2006; Helmy et al. 2013; Wirth et al. 2013; Junge et al. 2015).

IMPLICATIONS FOR PGE CONCENTRATION IN ORE DEPOSITS

The micro- to nanoscale investigation of platinum-group element-rich (PGE) base-metal sulfides (BMS) from the Caridad deposit in the Mayarí-Baracoa Ophiolite, eastern Cuba provides new insights into PGE partitioning during the formation of chromite ores in the mantle. Our observations link the formation of Ir-Pt nanoparticles with the crystallization of BMS, an occurrence that was not previously described in mantle-derived peridotites, nor in ore deposits. At the Caridad chromite deposit, the formation of Ir-Pt nanoparticles and nanodomains is attributed to two different processes: (1) exsolution of PGE from pentlandite during cooling (~610 °C), and (2) physical fractionation of Ir-Pt nanoparticles from a silicate melt, followed by entrainment into a sulfide melt. These observations suggest that, if noble metal nanoparticles can indeed precipitate from a silicate melt, the PGE content of a given sulfide assemblage may be significantly influenced by the physical incorporation of the nanoparticles into particular sulfides. Therefore, we suggest that the partitioning behavior of PGE, while predominantly controlled by equilibrium thermodynamics (i.e., partition coefficients), may be at least partly influenced by non-equilibrium kinetic and nanoscale effects (i.e., incorporation of metal nanoclusters). The mineralogical evidence provided in this paper, in addition to experimental observation of noble metal nanonuggets in silicate melts (e.g.,

Ballhaus et al. 2006; Anenburg and Mavrogenes 2016), highlight the importance of studying of solid inclusions in chromite ores to better understand the mechanism of fractionation of noble metals in magmatic systems.

ACKNOWLEDGMENTS

This research was financially supported by FEDER Funds through the projects CGL2015-65824-P and CGL2014-55949-R granted by the Spanish “Ministerio de Economía y Competitividad.” Additional funding was provided by the Millennium Science Initiative (MSI) grant “Millennium Nucleus for Metal Tracing along Subduction” (NC130065, Ministry of Economy, Chile). J.M.G.J. acknowledges financial support of the Ramón y Cajal Fellowship RYC-2015-17596 granted by the Spanish MINECO.

REFERENCES CITED

- Ahmed, A.H., and Arai, S. (2003) Platinum-group minerals in podiform chromitites of the Oman ophiolite. *Canadian Mineralogist*, 41, 597–616.
- Amossé J, Allibert, M., Fischer, W., and Piboule, M. (1990) Experimental study of the solubility of platinum and iridium in mafic silicate melts. Implications for the differentiation of platinum-group elements during magmatic processes. *Chemical Geology*, 81, 45–53.
- Anenburg, M., and Mavrogenes, J.A. (2016) Experimental observations on noble metal nanonuggets and Fe-Ti oxides, and the transport of platinum group elements in silicate melts. *Geochimica et Cosmochimica Acta*, 192, 258–278.
- Armstrong, J.T. (1988) Quantitative analysis of silicates and oxide minerals: Comparison of Monte-Carlo, ZAF and Phi-Rho-Z procedures. *Microbeam Analysis*, 239–246.
- Ballhaus, C. (1998) Origin of podiform chromite deposits by magma mingling. *Earth and Planetary Science Letters*, 156, 185–193.
- Ballhaus, C., and Sylvester, P. (2000) Noble metal enrichment processes in the Merensky Reef, Bushveld Complex. *Journal of Petrology*, 545–561.
- Ballhaus, C., Tredoux, M., and Späth, A. (2001) Phase relations in the Fe-Ni-Cu-PGE-S system at magmatic temperature and application to massive sulfide ores of the Sudbury igneous complex. *Journal of Petrology*, 42, 1911–1926.
- Ballhaus, C., Bockrath, C., Wohlgemuth-Ueberwasser, C., Laurenz, V., and Berndt, J. (2006) Fractionation of the noble metals by physical processes. *Contributions to Mineralogy and Petrology*, 152, 667–684.
- Barnes, S.J., and Ripley, E.M. (2016) Highly Siderophile and strongly chalcophile elements in magmatic ore deposits. *Reviews in Mineralogy and Geochemistry*, 81, 725–774.
- Bockrath, C., Ballhaus, C., and Holzheid, A. (2004) Stabilities of laurite RuS₂ and monosulphide liquid solution at magmatic temperature. *Chemical Geology*, 208, 265–271.
- Borisov, A., and Palme, H. (1995) The solubility of iridium in silicate melts: New data from experiments with Ir₉₀Pt₁₀ alloys. *Geochimica et Cosmochimica Acta*, 59, 481–485.
- (1997) Experimental determination of solubility of platinum in silicate melts. *Geochimica et Cosmochimica Acta*, 61, 4349–4357.
- Brenan, J.M., Cherniak, D.J., and Rose, L.A. (2000) Diffusion of osmium in pyrrhotite and pyrite; implications for closure of the Re–Os isotopic system. *Earth and Planetary Science Letters*, 180, 399–413.
- Cabri, L.J. (1973) New data on phase relations in the Cu-Fe-S system. *Economic Geology*, 64, 443–454.
- Chang, Y.A., and Hsieh, K.-C. (1986) Thermochemical description of the ternary iron nickel-sulphur system. In E. Ozberk and S.W. Marcuson, Eds., *Nickel Metallurgy: Extraction and Refining of Nickel*, 1, p. 248–277. Canadian Institute of Mining and Metallurgy.
- Craig, J.R. (1973) Pyrite-pentlandite assemblages and other low temperature relations in the Fe-Ni-S system. *American Journal of Science*, Cooper vol. 273-A, 496–510.
- Craig, J.R., and Kullerud, G. (1969) Phase relations in the Cu-Fe-Ni-S system and their application to magmatic ore deposits. *Economic Geology*, 4, 344–358.
- Donovan, J.J., and Tingle, T.N. (1996) An improved mean atomic number correction for quantitative microanalysis. *Journal of Microscopy*, 2, 1–7.
- Donovan, J.J., Snyder, D.A., and Rivers, M.L. (1993) An improved interference correction for trace element analysis. *Microbeam Analysis*, 2, 23–28.
- Donovan, J.J., Singer, J.W., and Armstrong, J.T. (2016) A new EPMA method for fast trace element analysis in simple matrices. *American Mineralogist*, 101, 1839–1853.
- Ebel, D.S., and Naldrett, A.J. (1996) Fractional crystallization of sulfide ore liquids at high temperature. *Economic Geology*, 91, 607–621.
- Fedorova, Z.N., and Sinyakova, E.F. (1993) Experimental investigation of physicochemical conditions of pentlandite formation. *Russian Journal of Geology and Geophysics*, 34, 79–87.
- Finnigan, C.S., Brenan, J.M., Mungall, J.E., and McDonough, W.F. (2008) Experiments and models bearing on the role of chromite as a collector of platinum group minerals by local reduction. *Journal of Petrology*, 49, 1647–1665.
- Fleet, M.E. (2006) Phase equilibria at high temperatures. *Reviews in Mineralogy and Geochemistry*, 61, 365–419.
- Fleet, M.E., and Pan, Y. (1994) Fractional crystallization of anhydrous sulfide liquid in the system Fe-Ni-Cu-S, with application to magmatic sulfide deposits. *Geochimica et Cosmochimica Acta*, 58, 3369–3377.
- Fleet, M.E., Crocket, J.H., Menghua, L., and Stone, W.E. (1999) Laboratory partitioning of platinum-group elements (PGE) and gold with application to magmatic sulfide-PGE deposits. *Lithos*, 47, 127–142.
- Fonseca, R.O.C., Brückel, K., Bragagni, A., Litzke, F., Speelmanns, I.M., and Wingwright, A.N. (2017) Fractionation of Rhenium from Osmium during noble metal alloy formation in association with sulfides: Implications for the interpretation of model ages in alloy-bearing magmatic rocks. *Geochimica et Cosmochimica Acta*, <http://dx.doi.org/10.1016/j.gca.2017.04.041>.
- Garuti, G., Zaccarini, F., and Economou-Eliopoulos, M. (1999) Paragenesis and composition of laurite from chromitites of Othrys (Greece): implications for Os–Ru fractionation in ophiolitic upper mantle of the Balkan Peninsula. *Mineralium Deposita*, 34, 312–319.
- Gervilla, F., Proenza, J.A., Frei, R., González-Jiménez, J.M., Garrido, C.J., Melgarejo, J.C., Meibom, A., Díaz-Martínez, R., and Lavaut, W. (2005) Distribution of platinum-group elements and Os isotopes in chromite ores from Mayarí-Baracoa Ophiolitic Belt (eastern Cuba). *Contributions to Mineralogy and Petrology*, 150, 589–607.
- González-Jiménez, J.M., and Reich, M. (2017) An overview of the platinum-group element nanoparticles in mantle-hosted chromite deposits. *Ore Geology Reviews*, 81, 1236–1248.
- González-Jiménez, J.M., Proenza, J.A., Gervilla, F., Melgarejo, J.C., Blanco-Moreno, J.A., Ruiz-Sánchez, R., and Griffin, W.L. (2011) High-Cr and high-Al chromitites from the Sagua de Tánamo district, Mayarí-Cristal Ophiolitic Massif (eastern Cuba): constraints on their origin from mineralogy and geochemistry of chromian spinel and platinum-group elements. *Lithos*, 125, 101–121.
- González-Jiménez, J.M., Gervilla, F., Griffin, W.L., Proenza, J.A., Augé, T., O'Reilly, S.Y., and Pearson, N.J. (2012) Os-isotope variability within sulfides from podiform chromitites. *Chemical Geology*, 291, 224–235.
- González-Jiménez, J.M., Villaseca, C., Griffin, W.L., O'Reilly, S.Y., Belousova, E., Ancochea, E., and Pearson, N.J. (2014) Significance of ancient sulfide PGE and Re–Os signatures in the mantle beneath Calatrava, Central Spain. *Contributions to Mineralogy and Petrology* 168, 1047, <https://doi.org/10.1007/s00410-014-1047-x>.
- González-Jiménez, J.M., Reich, M., Camprubi, A., Gervilla, F., Griffin, W.L., Colás, V., O'Reilly, S.Y., Proenza, J.A., Pearson, N.J., and Centeno-García, E. (2015) Thermal metamorphism of mantle chromitites and the stability of noble-metal nanoparticles. *Contributions to Mineralogy and Petrology*, 170, 15.
- Helmy, H.M., Ballhaus, C., Fonseca, R.O.C., Wirth, R., Nagel, T., and Tredoux, M. (2013) Noble metal nanoclusters and nanoparticles precede mineral formation in magmatic sulphide melts. *Nature Communications*, <http://dx.doi.org/10.1038/ncomms3405>.
- Hill, R., and Roeder, P. (1974) The crystallization of spinel from basaltic liquids as a function of oxygen fugacity. *Journal of Geology*, 82, 709–729.
- Holwell, D.A., Keays, R.R., McDonald, I., and Williams, M.R. (2015) Extreme enrichment of Se, Te, PGE and Au in Cu sulfide microdroplets: evidence from LA-ICP-MS analysis of sulphides in the Skaergaard Intrusion, east Greenland. *Contributions to Mineralogy and Petrology* 170 (53).
- Jugo, P.J. (2009) Sulfur content at sulfide saturation in oxidized magmas. *Geology*, 37, 415–418.
- Junge, M., Wirth, R., Oberthür, R., Melcher, F., and Schreiber, A. (2015) Mineralogical siting of platinum-group elements in pentlandite from the Bushveld Complex. South Africa. <http://dx.doi.org/10.1007/s00126-014-0561-0>.
- Kitakaze, A., Machida, T., and Komatsu, R. (2016) Phase relations in the Fe-Ni-S system from 875 to 650 °C. *Canadian Mineralogist*, 54, 1175–1186.
- Kogiso, T., Suzuki, K., Suzuki, T., and Uesugi, K. (2011) Two- and three-dimensional imaging of platinum-group minerals at submicrometer scale with synchrotron X-ray. *Goldschmidt Conference Abstracts 2008*, p. 1212, <https://goldschmidtabstracts.info/abstracts/abstractView?id=2011004927>.
- Kullerud, G. (1962) Two-liquid field in the Fe-S system. *Carnegie Institution of Washington, Year Book*, 60, 174–176.
- (1963) Thermal stability of pentlandite. *The Canadian Mineralogist*, 7, 353–366.
- Kullerud, G., and Yund, R.A. (1962) The Ni-S system and related minerals. *Journal of Petrology*, 3, 126–175.
- Laurenz, V., Fonseca, R.O., Ballhaus, C., Jochum, K.P., Heuser, A., and Sylvester, P.J. (2013) The solubility of palladium and ruthenium in picritic melts: 2. The effect of sulfur. *Geochimica et Cosmochimica Acta*, 108, 172–183.
- Li, C., Barnes, S.-J., Makovicky, E., Rose-Hansen, J., and Makovicky, M. (1996) Partitioning of nickel, copper, iridium, rhodium, platinum, and palladium between monosulfide solid solution and sulfide liquid: Effects of composition and temperature. *Geochimica et Cosmochimica Acta*, 60, 1231–1238.
- Lorand, J.-P., and Alard, O. (2001) Platinum-group element abundances in the upper mantle: New constraints from in situ and whole-rock analyses of Massif Central xenoliths (France). *Geochimica et Cosmochimica Acta*, 65, 2789–2806.
- Lorand, J.-P., Alard, O., and Luguet, A. (2010) Platinum-group element micronug-

- gets and refertilization process in Lherz orogenic peridotite (northeastern Pyrenees, France). *Earth and Planetary Science Letters*, 289, 298–310.
- Luguet, A., and Reissberg, L. (2016) Highly siderophile element and ¹⁸⁷Os signatures in non-cratonic basalt-hosted peridotite xenoliths: Unravelling the origin and evolution of the post-Archean lithospheric mantle. *Reviews in Mineralogy and Geochemistry*, 81, 305–367.
- Makovicky, M., Makovicky, E., and Rose-Hansen, J. (1986) Experimental studies on the solubility and distribution of platinum-group elements in base-metal sulphides in platinum deposits. In M.J. Gallagher, R.A. Ixer, C.R. Neary, and H.M. Prichard, Eds., *Metallogeny of Basic and Ultrabasic Rocks*, pp. 415–425. The Institution of Mining and Metallurgy, London, U.K.
- (1988) Experimental evidence of the formation and mineralogy of platinum and palladium ore deposits. In J. Boissonnas and P. Omenetto, Eds., *Mineral Deposits within the European Community*. Springer-Verlag, Berlin, Germany, pp. 303–317.
- Makovicky, E., Karup-Møller, S., Makovicky, M., and Rose-Hansen, J. (1990) Experimental studies on the phase systems Fe–Ni–Pd–S and Fe–Pt–Pd–As–S applied to PGE deposits. *Mineralogy and Petrology*, 42, 307–319.
- Malitch, K.N., Melcher, F., and Mühlhans, H. (2001) Palladium and gold mineralization in podiform chromitite at Kraubath, Austria. *Mineralogy and Petrology*, 73, 247–277.
- Marchesi, C., Garrido, C.J., Godard, M., Proenza, J.A., Gervilla, F., and Blanco-Moreno, J. (2006) Petrogenesis of highly depleted peridotites and gabbroic rocks from the Mayarí-Baracoa Ophiolitic Belt (eastern Cuba). *Contributions to Mineralogy and Petrology*, 151, 717–736.
- Marchesi, C., Garrido, C.J., Boch, D., Proenza, J.A., Gervilla, F., Monié, P., and Rodríguez-Vega, A. (2007) Geochemistry of Cretaceous magmatism in eastern Cuba: recycling of North American continental sediments and implications for Subduction Polarity in the Greater Antilles Paleo-Arc. *Journal of Petrology*, 48, 1813–1840.
- Marchesi, G., González-Jiménez, J.M., Gervilla, F., Garrido, C.J., Griffin, W.L., O'Reilly, S.Y., Proenza, J.A., and Pearson, N.J. (2011) In situ Re–Os isotopic analysis of platinum-group minerals from the Mayarí-Cristal ophiolitic massif (Mayarí-Baracoa Ophiolitic Belt, eastern Cuba): Implications for the origin of Os-isotope heterogeneities in podiform chromitites. *Contributions to Mineralogy and Petrology*, 161, 977–990.
- Matveev, S., and Ballhaus, C. (2002) Role of water in the origin of podiform chromitite deposits. *Earth and Planetary Science Letters*, 203, 235–243.
- Melcher, F., Grum, W., Simon, G., Thalhammer, T.V., and Stumpfl, E.F. (1997) Petrogenesis of the ophiolitic giant chromite deposits of Kempirsai, Kazakhstan: a study of solid and fluid inclusions in chromite. *Journal of Petrology*, 38, 1419–1458.
- Misra, K.C., and Fleet, M.E. (1973) The chemical compositions of synthetic and natural pentlandite assemblages. *Economic Geology*, 68, 518–539.
- Mungall, J.E. (2005) Magmatic geochemistry of the platinum-group elements. In J.E. Mungall, Ed., *Exploration from Platinum-Group Elements Deposits: Short Course Series*, 35, p. 1–34. Mineralogical Association of Canada.
- Mungall, J.E., Andrews, D.R.A., Cabri, L.J., Sylvester, P.J., and Tubrett, M. (2005) Partitioning of Cu, Ni, Au, and platinum-group elements between monosulfide solid solution and sulfide melt under oxygen and sulfur fugacities. *Geochimica et Cosmochimica Acta*, 69, 4349–4360.
- Naldrett, A.J., Lehmann, J., and Augé, T. (1989) Spinel non-stoichiometry and reactions between chromite and closely associated sulphides, with examples from ophiolite complexes. In M.D. Predergast and J. Jones, Eds., *Magmatic Sulphides—The Zimbabwe volume*. The Institution of Mining and Metallurgy, London, p. 221–227.
- Naldrett, A.J., Kinnaird, J., Wilson, A., Yudovskaya, M., McQuade, S., Chunnett, G., and Stanley, C. (2009) Chromite composition and PGE content of Bushveld chromitites: Part 1—the lower and middle groups. *Transactions of the Institutions of Mining and Metallurgy: Section B*, 118, 131–161.
- Pearson, N.J., Alard, O., Griffin, W.L., Jackson, S.E., and O'Reilly, S.Y. (2002) In situ measurement of Re–Os isotopes in mantle sulfides by laser ablation multicollector-inductively coupled plasma mass spectrometry: analytical methods and preliminary results. *Geochimica et Cosmochimica Acta*, 66, 1037–1050.
- Peregoedova, A.V., Barnes, S.J., and Baker, D.R. (2004) The formation of Pt–Ir alloys and Cu–Pd-rich sulfide melts by partial desulfurization of Fe–Ni–Cu sulfides: Results of experiments and implications for natural systems. *Chemical Geology*, 208, 247–264.
- Piña, R., Gervilla, F., Barnes, S.J., Ortega, L., and Lunar, R. (2012) Distribution of platinum-group and chalcophile elements in the Aguablanca Ni–Cu sulfide deposit (SW Spain): Evidence from a LA-ICP-MS study. *Chemical Geology*, 302–303, 61–75.
- (2016) Platinum-group element concentration in pyrite from the main sulfide zone of the Great Dyke of Zimbabwe. *Mineralium Deposita*, 51, 853–872.
- Proenza, J.A., Gervilla, F., Melgarejo, J.C., and Bodinier, J.L. (1999) Al- and Cr-rich chromitites from the Mayarí-Baracoa Ophiolitic Belt (eastern Cuba): consequence of interaction between volatile-rich melts and peridotite in suprasubduction mantle. *Economic Geology*, 94, 547–566.
- Proenza, J.A., Alfonso, P., Melgarejo, J.C., Gervilla, F., Tritilla, J., and Fallick, A.E. (2003) D, O, and C isotopes in podiform chromitites as fluid tracers for hydrothermal alteration processes of the Mayarí-Baracoa Ophiolitic Belt, eastern Cuba. *Journal of Geochemical Exploration* 78–79, 1–6.
- Proenza, J.A., Díaz-Martínez, R., Iriondo, A., Marchesi, C., Melgarejo, J.C., Gervilla, F., Garrido, C.J., Rodríguez-Vega, A., Lozano-Santacruz, R., and Blanco-Moreno, J.A. (2006) Primitive island-arc Cretaceous volcanic rocks in eastern Cuba: The Téneme Formation. *Geologica Acta*, 4, 103–121.
- Reich, M., Utsunomiya, S., Kesler, S.E., Wang, L.M., Ewing, R.C., and Becker, U. (2006) Thermal behavior of metal nanoparticles in geologic materials. *Geology*, 34, 1033–1036.
- Saunders, J.E., Pearson, N.J., O'Reilly, S.Y., and Griffin, W.L. (2015) Sulfide metasomatism and the mobility of gold in the lithospheric mantle. *Chemical Geology*, 410, 149–161.
- Shewman, R.W., and Clark, L.A. (1970) Pentlandite phase relations in the Fe–Ni–S system and notes on the monosulfide solid solution. *Canadian Journal of Earth Science*, 7, 67–85.
- Sugaki, A., and Kitakaze, A. (1998) High form of pentlandite and its thermal stability. *American Mineralogist*, 83, 133–140.
- Tassara, C.S., González-Jiménez, J.M., Reich, M., Schilling, M., Morata, D., Begg, G., Saunders, J.E., Griffin, W.L., O'Reilly, S.Y., Gregoire, M., Barra, F., and Corgne, A. (2017) Plume-subduction interaction forms large auriferous provinces. *Nature Communications*, 8, DOI: 10.1038/s41467-017-00821-z.
- Tolstikh, N.D., Foley, J.Y., Sidorov, E.G., and Laajoki, K.V.O. (2002) Composition of the platinum-group minerals in the Salmon River placer deposit, Goodnews Bay, Alaska. *Canadian Mineralogist*, 40, 463–471.
- Tredoux, M., Lindsay, N.M., Davies, G., and McDonald, I. (1995) The fractionation of platinum-group elements in magmatic systems with the suggestion of a novel causal mechanism. *South African Journal of Geology*, 98, 157–167.
- Turchi, P.E.A., Drchal, V., and Kudronovskiy, J. (2006) Stability and ordering properties of fcc alloys based on Rh, Ir, Pd and Pt. *Physical Review B*, 74, 064202.
- Wang, K.L., O'Reilly, S.Y., Griffin, W.L., Pearson, N.J., and Zhang, M. (2009) Sulfides in mantle peridotites from Penghu Island, Taiwan: melt percolation, PGE fractionation, and the lithospheric evolution of the South China block. *Geochimica et Cosmochimica Acta*, 73, 4531–4557.
- Wirth, R., Reid, D., and Schreiber, A. (2013) Nanometer-sized platinum-group minerals (PGM) in base metal sulfides: new evidence for an orthomagmatic origin of the Merensky reef PGE ore deposit. Bushveld Complex. *South Africa. Canadian Mineralogist*, 5, 143–155.
- Wood, S.A. (1987) Thermodynamic calculations of the volatility of the platinum group elements (PGE): The PGE content of fluids at magmatic temperatures. *Geochimica et Cosmochimica Acta*, 61, 3041–3050.

MANUSCRIPT RECEIVED DECEMBER 7, 2017

MANUSCRIPT ACCEPTED APRIL 18, 2018

MANUSCRIPT HANDLED BY KYLE ASHLEY

Endnote:

¹Deposit item AM-18-86424, Supplemental Table. Deposit items are free to all readers and found on the MSA web site, via the specific issue's Table of Contents (go to http://www.minsocam.org/MSA/AmMin/TOC/2018/Aug2018_data/Aug2018_data.html).